Contact analysis within the bi-potential framework using cell-based smoothed finite element method

Qianwei Chen, Yan Li, Zhiqiang Feng, Huijian Chen

Contact analysis within the bi-potential framework using cell-based smoothed finite element method

***Qianwei Chen[1], †Yan Li[1], Zhiqiang Feng[1,2] and Huijian Chen[1]**

[1]School of Mechanics and Engineering, Southwest Jiaotong University, Chengdu, China
[2] LMEE Univ-Evry, Université Paris-Saclay, Evry, France

*Presenting author: qwchen0110@163.com
†Corresponding author: liyan001de@gmail.com

Abstract

This paper presents a cell-based smoothed finite element method (CS-FEM) for solving two-dimensional contact problems with the bi-potential formulation. The contact force and the relative displacement are coupled with each other and solved by Uzawa algorithm. Three contact states are investigated accurately. The CS-FEM is performed with six different kinds of smoothing domains which are constructed by dividing the background element into different regions. Three numerical examples are presented to verify the accuracy of the method. The effect of the friction coefficient for the contact are also investigated. All solutions agree well with reference values. The results produced by the CS-FEM are more accurate than those of the traditional FEM. Besides, the CS-FEM can provide both upper bound and lower bound solutions for the strain energy while using different smoothing domains.

Keywords: Contact analysis, CS-FEM, Bi-potential formulation, Uzawa algorithm

1. Introduction

The contact problems exist everywhere in life. For example, the contact between the tire and the road, the contact between the shaft and the bearing, the contact between the knife and the flesh in virtual surgery, etc. They play important roles in many engineering applications [1][2].

There are two reasons contributed to the non-linearity of the contact problems [3][4]. One is that both the contact surfaces and their positions change during the contact process. The other one is the non-linearity of contact conditions, including the non-penetration of contact bodies and the tangential friction conditions. The widely used contact algorithms in engineering applications are the penalty function method [5]-[8], the Lagrange multiplier method [9]-[12] and the linear complementarity techniques [13]-[16]. The bi-potential method proposed by De Saxcé and Feng provides an effective tool for dissipative constitutive modelling [17][18]. Applying the augmented Lagrangian method to the law of contact, the implicit equation of the projection on the Coulomb's cone is equivalent to the original contact inequality. There has demonstrated that the Uzawa algorithm is more efficient when compared with the Newton method [19]. There are many researches and applications in impact, hyperelasticity, wear and other problems [20]-[23].

The finite element method (FEM) is one of the most effective numerical methods for solving contact problems. Other widely used approaches include the boundary element methods [24][25] and the meshless methods [26]-[28]. The smoothed finite element method (S-FEM) proposed by Liu et al. is a weakened weak form method based on the G-space theory [29]. When using different kinds of smoothing domains which are based on cells, edges, nodes and faces of the background elements, the cell-based smoothed finite element method (CS-FEM),

the edge-based smoothed finite element method, the node-based smoothed finite element method and the face-based smoothed finite element method are created [30]-[33]. So far, the S-FEM has been widely used in various fields, including the acoustics [34], materials science [35], vibration [36], fluid-structure coupling [37], and electromagnetics [38]. The S-FEM has also been applied to solve contact problems [16][26][39][40].

In this paper, the CS-FEM with quadrilateral elements is used to solve the two-dimensional contact problems within the bi-potential framework. The contact forces can be solved using the Uzawa algorithm. The rest of the paper is organized as follows: in Section 2, the governing equations and the contact criterion are introduced. Section 3 illustrates the smoothed finite element method, especially the CS-FEM. The smoothed Galerkin weak form is obtained by using the smoothing strain technique. In Section 4, the contact analysis is performed within the bi-potential framework. The Uzawa algorithm is applied to solve the contact force. Finally, three numerical examples are presented to examine the numerical accuracy of the proposed method.

2. Problem statement

2.1 *Governing equations*

Considering an elastic contact body with domain Ω_i and the force boundary condition Γ_f^i, the displacement boundary condition Γ_u^i, the contact boundary condition Γ_c^i as shown in Fig. 1.

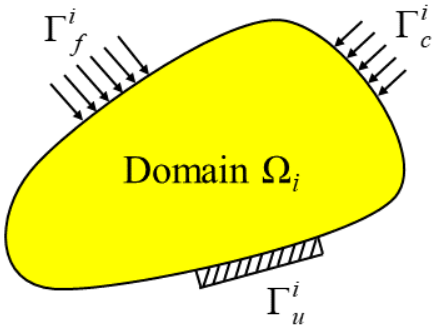

Figure 1. Contact body

The governing equation of this contact body is:

$$\nabla^{\mathrm{T}}\boldsymbol{\sigma}+\mathbf{f}=0 \tag{1}$$

with

$$\begin{cases}\mathbf{L}^{\mathrm{T}}\boldsymbol{\sigma}=\bar{\mathbf{t}} & \text{on } \Gamma_f \\ \mathbf{L}^{\mathrm{T}}\boldsymbol{\sigma}=\bar{\mathbf{r}} & \text{on } \Gamma_c \\ \mathbf{u}=\bar{\mathbf{u}} & \text{on } \Gamma_u\end{cases} \tag{2}$$

where ∇ is a differential operator which can be written for 2D problems as follows:

$$\nabla=\begin{bmatrix}\partial/\partial x & 0 \\ 0 & \partial/\partial y \\ \partial/\partial y & \partial/\partial x\end{bmatrix} \tag{3}$$

The stress $\boldsymbol{\sigma}=\left[\sigma_{xx}\ \ \sigma_{yy}\ \ \tau_{xy}\right]^{\mathrm{T}}$. The body force $\mathbf{f}=\left[f_x\ \ f_y\right]^{\mathrm{T}}$ and displacements $\mathbf{u}=\left[u_x\ \ u_y\right]^{\mathrm{T}}$. $\bar{\mathbf{t}}$, $\bar{\mathbf{u}}$ and $\bar{\mathbf{r}}$ are the loads, displacements and contact forces on the boundary, respectively. $\mathbf{L}$ is the matrix of the unit normal vectors defined by:

$$\mathbf{L}=\begin{bmatrix}\partial x/\partial n & 0\\ 0 & \partial y/\partial n\\ \partial y/\partial n & \partial x/\partial n\end{bmatrix}. \tag{4}$$

2.2 *Contact criterion*

The Signorini condition mainly describes a normal contact relationship. It has the following three characteristics at each contact point, they are the geometric condition of non-penetration, the static condition of non-adhesion and the mechanical complementary condition. Therefore, the following formula expresses the relationship between the normal distance x_n^α and normal contact force r_n^α for any contact point α. The Signorini condition is defined as:

$$Signor(x_n^\alpha, r_n^\alpha) \ \Leftrightarrow \begin{cases} x_n^\alpha \ge 0 \\ r_n^\alpha \ge 0 \quad x_n^\alpha r_n^\alpha = 0 \end{cases} \tag{5}$$

In order to satisfy the tangential criterion of contact, the Coulomb friction rule is adopted and:

$$Coul(\mathbf{x}_t^\alpha, \mathbf{r}_t^\alpha) \ \Leftrightarrow \begin{cases} \left\|\mathbf{x}_t^\alpha\right\| = 0 \quad \left\|\mathbf{r}_t^\alpha\right\| \le \mu r_n^\alpha \\ \left\|\mathbf{x}_t^\alpha\right\| \ne 0 \quad \mathbf{r}_t^\alpha = -\mu r_n^\alpha \dfrac{\mathbf{x}_t^\alpha}{\left\|\mathbf{x}_t^\alpha\right\|} \end{cases} \tag{6}$$

where $\mathbf{x}_t^\alpha$ and $\mathbf{r}_t^\alpha$ are the tangential components of the spacing vector and the contact force vector for contact point α, respectively. μ is the friction coefficient.

Let K_μ represents the Coulomb's cone which is expressed as:

$$K_\mu = \left\{\mathbf{r} \in \mathbb{R}3 \ \text{ such that } \ \left\|\mathbf{r}_t^\alpha\right\| - \mu r_n^\alpha \le 0\right\} \tag{7}$$

The contact satisfies a complex non-smooth dissipative law including the separating, sticking and sliding. By combining Eqs. (5) and (7), the contact criterion can be written as:

$$\begin{aligned} &Separating: x_n^\alpha > 0 \quad \text{and } \mathrm{r}_n^\alpha = 0 \\ &Sticking: \left\|\mathbf{x}_t^\alpha\right\| = 0 \text{ and } \mathbf{r}_t^\alpha \in \mathrm{int}(K_\mu) \\ &Sliding: \left\|\mathbf{x}_t^\alpha\right\| \ne 0 \text{ and } \mathbf{r}_t^\alpha \in \mathrm{bd}(K_\mu) \text{ with } \mathbf{r}_t^\alpha = -\mu r_n^\alpha \frac{\mathbf{x}_t^\alpha}{\left\|\mathbf{x}_t^\alpha\right\|} \end{aligned} \tag{8}$$

where $\mathrm{int}(K_\mu)$ and $\mathrm{bd}(K_\mu)$ represent the interior and the boundary of Coulomb's cone. Eq. (8) is called the Signorini-Coulomb conditions.

3. Cell-based smoothed finite element method

3.1 *Galerkin weak form*

For problem domain Ω, by introducing a weight function $\boldsymbol{\varphi}$, Eq. (1) can be transformed into an equivalent integral form:

$$\int_\Omega \boldsymbol{\varphi}^{\mathrm{T}} \nabla^{\mathrm{T}} \boldsymbol{\sigma} \mathrm{d}\Omega + \int_\Omega \boldsymbol{\varphi}^{\mathrm{T}} \mathbf{f} \mathrm{d}\Omega = 0 \tag{9}$$

Using Green's divergence theorem, we can convert Eq. (9) to:

$$\int_\Omega (\nabla \boldsymbol{\varphi})^{\mathrm{T}} \mathbf{C}\boldsymbol{\varepsilon} \mathrm{d}\Omega - \int_\Omega \boldsymbol{\varphi}^{\mathrm{T}} \mathbf{f} \mathrm{d}\Omega - \int_{\Gamma_f} \boldsymbol{\varphi}^{\mathrm{T}} \bar{\mathbf{t}} \mathrm{d}\Gamma - \int_{\Gamma_c} \boldsymbol{\varphi}^{\mathrm{T}} \bar{\mathbf{r}} \mathrm{d}\Gamma = 0 \tag{10}$$

where $\mathbf{C}$ is the material matrix. The physical equation is $\boldsymbol{\sigma}=\mathbf{C}\boldsymbol{\varepsilon}$, where $\boldsymbol{\varepsilon}$ is the vector of strain. The weight function takes the variation of displacement as $\boldsymbol{\varphi} = \delta\mathbf{u}$ and the Galerkin weak form can be got:

$$\int_\Omega (\delta\boldsymbol{\varepsilon})^{\mathrm{T}} \mathbf{C}\boldsymbol{\varepsilon} \mathrm{d}\Omega - \int_\Omega \left(\delta\mathbf{u}\right)^{\mathrm{T}} \mathbf{f} \mathrm{d}\Omega - \int_{\Gamma_f} \left(\delta\mathbf{u}\right)^{\mathrm{T}} \bar{\mathbf{t}} \mathrm{d}\Gamma - \int_{\Gamma_c} \left(\delta\mathbf{u}\right)^{\mathrm{T}} \bar{\mathbf{r}} \mathrm{d}\Gamma = 0 \tag{11}$$

where $\delta\boldsymbol{\varepsilon} = \nabla\delta\mathbf{u}$.

3.2 *Smoothed Galerkin weak form*

In S-FEM, the smoothed strain $\bar{\boldsymbol{\varepsilon}}$ is calculated by the strain smoothing operation as:

$$\bar{\boldsymbol{\varepsilon}}(\bar{\mathbf{x}}) = \int_{\Omega_s} \boldsymbol{\varepsilon}(\mathbf{x}) W(\bar{\mathbf{x}} - \mathbf{x}) \mathrm{d}\Omega \tag{12}$$

where Ω_s is the smoothing domain which can be created based on nodes, edges, cells of the background elements. In this work the CS-FEM model is adopted with six different kinds of smoothing regions as shown in Fig. 2. W is a smoothing function that should be positive over the local support domain and satisfies the unity property $\int_{\Omega_s} W(\bar{\mathbf{x}} - \mathbf{x}) \mathrm{d}\Omega = 1$.

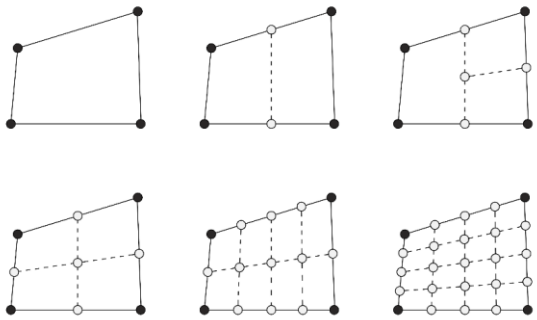

Figure 2. Six different smoothing domains based on a quadrilateral element: 1SD, 2SDs, 3SDs, 4SDs, 8SDs, 16SDs

Here the Heaviside-type smoothing function is adopted:

$$W(\bar{\mathbf{x}} - \mathbf{x}) = \begin{cases} 1/\bar{A} & \mathbf{x} \in \Omega_s \\ 0 & \mathbf{x} \notin \Omega_s \end{cases} \tag{13}$$

where $\bar{A}$ is the area of the smoothing domain. Substituting Eq. (13) into Eq. (12) and using the Green's divergence theorem, the smoothed strain can be obtained:

$$\begin{aligned} \bar{\boldsymbol{\varepsilon}} &= \int_{\Omega_s} \nabla\mathbf{u} W(\bar{\mathbf{x}} - \mathbf{x}) \mathrm{d}\Omega \\ &= -\int_{\Omega_s} \nabla W(\bar{\mathbf{x}} - \mathbf{x}) \mathbf{u} \mathrm{d}\Omega + \frac{1}{\bar{A}} \int_{\Gamma_s} \mathbf{L}\mathbf{u} \mathrm{d}\Gamma \\ &= \frac{1}{\bar{A}} \int_{\Gamma_s} \mathbf{L}\mathbf{u} \mathrm{d}\Gamma \end{aligned} \tag{14}$$

where Γ_s is the boundary of the smoothing domain. Note that only boundary integration instead of domain integral is required in this calculation.

By substituting Eq. (14) into Eq. (11), the following smoothed Galerkin weak form can be obtained:

$$\int_{\Omega}(\delta\bar{\boldsymbol{\varepsilon}})^{\mathrm{T}}\mathbf{C}\bar{\boldsymbol{\varepsilon}}\mathrm{d}\Omega-\int_{\Omega}\left(\delta\mathbf{u}\right)^{\mathrm{T}}\mathbf{f}\mathrm{d}\Omega-\int_{\Gamma_f}\left(\delta\mathbf{u}\right)^{\mathrm{T}}\bar{\mathbf{t}}\mathrm{d}\Gamma-\int_{\Gamma_c}\left(\delta\mathbf{u}\right)^{\mathrm{T}}\bar{\mathbf{r}}\mathrm{d}\Gamma=0 \tag{15}$$

3.3 *Discretized system of equations*

Assume the displacement function as:

$$\mathbf{u(x)=N(x)d}\quad \mathbf{x}\in\Omega_s \tag{16}$$

where vector $\mathbf{N(x)}$ and $\mathbf{d}$ represent the shape function and nodal displacements respectively.

Substituting Eq. (16) into Eq. (14), the smoothing strain $\bar{\boldsymbol{\varepsilon}}$ can be written as:

$$\bar{\boldsymbol{\varepsilon}}=\frac{1}{\bar{A}}\int_{\Gamma_s}\mathbf{Lu}\mathrm{d}\Gamma=\bar{\mathbf{B}}\mathbf{d} \tag{17}$$

where $\bar{\mathbf{B}}$ denotes the smoothed strain matrix which can be calculated as:

$$\bar{\mathbf{B}}=\frac{1}{\bar{A}}\int_{\Gamma_s}\mathbf{LN(x)}\mathrm{d}\Gamma=\begin{bmatrix}\bar{b}_x & 0\\ 0 & \bar{b}_y\\ \bar{b}_y & \bar{b}_x\end{bmatrix}\quad \mathbf{x}\in\Gamma_s \tag{18}$$

with

$$\bar{b}_h=\frac{1}{\bar{A}}\sum_{p=1}^{N_p}n_{h,p}\mathbf{N}(\mathbf{x}_p^G)l_p\quad h=x,y \tag{19}$$

where N_p represents the number of segments of the boundary Γ_s, $n_{h,p}$ and $\mathbf{x}_p^G$ are respectively the outward unit normal and Gauss points on each segment, l_p represents the length of the p-th segment.

Substituting Eq. (16) and Eq. (17) into Eq. (15), we can get the discretized algebraic system of equations:

$$\sum_{e=1}^{N_e}\sum_{s=1}^{N_s}\bar{A}_s\bar{\mathbf{B}}^{\mathrm{T}}\mathbf{C}\bar{\mathbf{B}}\mathbf{d}-\sum_{e=1}^{N_e}\int_{\Omega_e}\mathbf{N}^{\mathrm{T}}\mathbf{f}\mathrm{d}\Omega-\sum_{e=1}^{N_e}\int_{\Gamma_{ef}}\mathbf{N}^{\mathrm{T}}\bar{\mathbf{t}}\mathrm{d}\Gamma-\sum_{e=1}^{N_e}\int_{\Gamma_{ec}}\mathbf{N}^{\mathrm{T}}\bar{\mathbf{r}}\mathrm{d}\Gamma=0 \tag{20}$$

where N_e and N_s represent the number of background elements and smoothing domains. Ω_e represents background element. Γ_{ef} and Γ_{ec} represent the boundary of forces and contact forces per element. For simplicity of description, we can use the following symbols:

$$\mathbf{F}_{ext}=\sum_{e=1}^{N_e}\int_{\Omega_e}\mathbf{N}^{\mathrm{T}}\mathbf{f}\mathrm{d}\Omega+\sum_{e=1}^{N_e}\int_{\Gamma_{ef}}\mathbf{N}^{\mathrm{T}}\bar{\mathbf{t}}\mathrm{d}\Gamma \tag{21}$$

$$\mathbf{R}=\sum_{e=1}^{N_e}\int_{\Gamma_{ec}}\mathbf{N}^{\mathrm{T}}\bar{\mathbf{r}}\mathrm{d}\Gamma \tag{22}$$

$$\mathbf{F}_{int}=\sum_{e=1}^{N_e}\sum_{s=1}^{N_s}\bar{A}_s\bar{\mathbf{B}}^{\mathrm{T}}\mathbf{C}\bar{\mathbf{B}}\mathbf{d} \tag{23}$$

where $\mathbf{F}_{ext}$ is the external forces. $\mathbf{R}$ is the contact forces. $\mathbf{F}_{int}$ is the internal forces.

The Eq. (20) can be rewritten as:

$$\bar{\mathbf{K}}\mathbf{d}=\mathbf{F}_{ext}+\mathbf{R} \tag{24}$$

where $\bar{\mathbf{K}}$ is stiffness matrix obtained by:

$$\bar{\mathbf{K}}=\sum_{e=1}^{N_e}\sum_{s=1}^{N_s}\bar{A}_s\bar{\mathbf{B}}^{\mathrm{T}}\mathbf{C}\bar{\mathbf{B}} \tag{25}$$

Here Eq. (24) cannot be solved directly because both $\mathbf{d}$ and $\mathbf{R}$ are unknown quantities. In our work we compute the contact force $\mathbf{R}$ on the contact surface first. Then the displacements $\mathbf{d}$ can be solved by taking $\mathbf{R}$ as an external force.

4. The contact within the bi-potential framework

4.1 *Contact kinematics*

Considering two elastic bodies Ω_1 and Ω_2 coming into contact, as shown in Fig. 3. P_1 is the contact points on the boundary Γ_1. P_2 is the normal projection point of the contact point P_1 on the boundary Γ_2. For 2D problems, we can set up a local coordinate system based on the normal and tangential vector at point P_1. The initial gap $\mathbf{g}$ between P_1 and P_2 is determined by a contact collision detector as shown in Fig. 3:

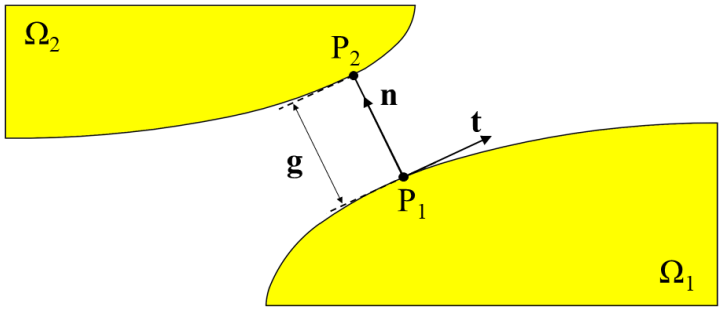

Figure 3. Contact kinematics

Assuming:

$$\mathbf{d}(\mathrm{P}_1)=\mathbf{\Phi}_1\mathbf{d}_1 \quad \mathbf{d}(\mathrm{P}_2)=\mathbf{\Phi}_2\mathbf{d}_2 \tag{26}$$

where $\mathbf{d}_1$ and $\mathbf{d}_2$ denotes respectively the nodal displacements in Ω_1 and Ω_2. $\mathbf{\Phi}_1$ and $\mathbf{\Phi}_2$ are integration matrix in corresponding regions. If we consider the case with N_c contact points $\mathrm{P}_1^\alpha \ (\alpha=1\cdots N_c)$ on Γ_1, and P_2^α is the normal projection points of the contact points P_1^α on Γ_2. The relative position between P_1^α and P_2^α is:

$$\mathbf{d}^\alpha=\mathbf{d}(\mathrm{P}_2^\alpha)-\mathbf{d}(\mathrm{P}_1^\alpha) \tag{27}$$

In local coordinates it can be expressed as:

$$\mathbf{d}^\alpha=x_t^\alpha\mathbf{t}+x_n^\alpha\mathbf{n} \tag{28}$$

where

$$\mathbf{x}^\alpha=\begin{Bmatrix}x_t^\alpha\\x_n^\alpha\end{Bmatrix}=\begin{Bmatrix}\mathbf{t}^{\mathrm{T}}\mathbf{d}^\alpha\\\mathbf{n}^{\mathrm{T}}\mathbf{d}^\alpha\end{Bmatrix}. \tag{29}$$

Substituting Eq. (26) and Eq. (27) to Eq. (29), we get:

$$\begin{Bmatrix}x_t^\alpha\\x_n^\alpha\end{Bmatrix}=\begin{bmatrix}-\mathbf{t}^{\mathrm{T}}\mathbf{\Phi}_1 & 0 & \mathbf{t}^{\mathrm{T}}\mathbf{\Phi}_2 & 0\\ 0 & -\mathbf{n}^{\mathrm{T}}\mathbf{\Phi}_1 & 0 & \mathbf{n}^{\mathrm{T}}\mathbf{\Phi}_2\end{bmatrix}\begin{Bmatrix}\mathrm{d}_{1x}\\\mathrm{d}_{1y}\\\mathrm{d}_{2x}\\\mathrm{d}_{2y}\end{Bmatrix} \tag{30}$$

By defining the transformation matrix $\mathbf{T}$ as:

$$\mathbf{T}^\alpha=\left[-\mathbf{T}_1^\alpha\middle|\mathbf{T}_2^\alpha\right] \quad \mathbf{T}_k^\alpha=\begin{bmatrix}\mathbf{t}^{\mathrm{T}}\mathbf{\Phi}_k & 0\\ 0 & \mathbf{n}^{\mathrm{T}}\mathbf{\Phi}_k\end{bmatrix} \tag{31}$$

Eq. (30) can be written as:

$$\mathbf{x}^{\alpha} = \mathbf{T}^{\alpha}\mathbf{d} \tag{32}$$

whose incremental form is:

$$\mathbf{x}^{\alpha(i+1)} = \mathbf{T}^{\alpha}\mathbf{d}^{(i)} + \mathbf{g}^{\alpha} \tag{33}$$

where $\mathbf{g}^{\alpha} = (0 \;\; g^{\alpha})$.

In the local reference coordinate system, the contact force $\mathbf{r}^{\alpha}$ can be defined as:

$$\mathbf{r}^{\alpha} = r_t^{\alpha}\mathbf{t} + r_n^{\alpha}\mathbf{n} \tag{34}$$

Applying the contact virtual work principle:

$$\mathbf{r}^{\alpha\mathrm{T}}\delta\mathbf{x}^{\alpha} = \mathbf{R}^{\alpha\mathrm{T}}\delta\mathbf{d}^{\alpha} \tag{35}$$

We have:

$$\mathbf{R}^{\alpha} = \mathbf{T}^{\alpha\mathrm{T}}\mathbf{r}^{\alpha} \tag{36}$$

The whole system of equations of N_c contact points can be written as:

$$\begin{cases} \mathbf{R} = \mathbf{T}^{\mathrm{T}}\mathbf{r} \\ \mathbf{x} = \mathbf{T}\mathbf{d} + \mathbf{g} \end{cases} \tag{37}$$

with $\mathbf{T} = \begin{bmatrix} \mathbf{T}^1 & \cdots & \mathbf{T}^{\alpha} \end{bmatrix}^{\mathrm{T}}$, $\mathbf{x} = \begin{bmatrix} \mathbf{x}^1 & \cdots & \mathbf{x}^{N_C} \end{bmatrix}^{\mathrm{T}}$, $\mathbf{r} = \begin{bmatrix} \mathbf{r}^1 & \cdots & \mathbf{r}^{N_C} \end{bmatrix}^{\mathrm{T}}$, $\mathbf{g} = \begin{bmatrix} \mathbf{g}^1 & \cdots & \mathbf{g}^{N_C} \end{bmatrix}^{\mathrm{T}}$.

4.2 *The contact solution method*

For a contact point, the bi-potential function of the contact law can be written as:

$$b_c(-\mathbf{x}^{\alpha}, \mathbf{r}^{\alpha}) = \prod_{\mathbb{R}_-}(-x_n^{\alpha}) + \prod_{K_{\mu}}(\mathbf{r}^{\alpha}) + \mu r_n^{\alpha}\left\|\mathbf{x}_t^{\alpha}\right\| \tag{38}$$

where $\mathbb{R}_- = (-\infty, 0]$, and $\prod_{K_{\mu}}(\mathbf{r}^{\alpha})$ is the indicator function and it can be described as: if $\mathbf{r}^{\alpha} \in K_{\mu}$, $\prod_{K_{\mu}}(\mathbf{r}^{\alpha}) = 0$; otherwise $\prod_{K_{\mu}}(\mathbf{r}^{\alpha}) = +\infty$.

The Eq. (38) can be further expressed as an implicit subnormal form:

$$\begin{aligned} -\mathbf{x}^{\alpha} &\in \frac{\partial b_c(-\mathbf{x}^{\alpha}, \mathbf{r}^{\alpha})}{\partial r^{\alpha}} \\ \mathbf{r}^{\alpha} &\in \frac{\partial b_c(-\mathbf{x}^{\alpha}, \mathbf{r}^{\alpha})}{\partial(-x^{\alpha})} \end{aligned} \tag{39}$$

So, using the augmented Lagrangian method [41], the Eq. (38) and Eq. (39) can be equivalent to the following projection form on the Coulomb's cone:

$$\mathbf{r}^{\alpha} = \mathrm{Proj}_{K_{\mu}}(\mathbf{r}^{\alpha*}) \tag{40}$$

where $\mathbf{r}^{\alpha*}$ represents the vector of augmented contact force, and it is given by:

$$\mathbf{r}^{\alpha*} = \mathbf{r}^{\alpha} - \rho\mathbf{x}^{\alpha*} \;\; \text{with} \; \mathbf{x}^{\alpha*} = \mathbf{x}^{\alpha} + \mu\left\|\mathbf{x}_t^{\alpha}\right\|\mathbf{n}^{\alpha} \tag{41}$$

where ρ is the bi-potential coefficient. In this work, the reciprocal of the maximum value of the diagonal elements of the matrix $\mathbf{D}$ as given in Eq. (45) is selected.

By summarizing the above equations and Eq. (8), there will be three contact situations within the bi-potential framework. They are $\mathbf{r}^{\alpha*} \in K_{\mu}$ (sticking), $\mathbf{r}^{\alpha*} \in K_{\mu}^{*}$ (separating) and $\mathbf{r}^{\alpha*} \in \mathbb{R}^2 - (K_{\mu} \bigcup K_{\mu}^{*})$ (sliding), respectively, as shown in Fig. 4.

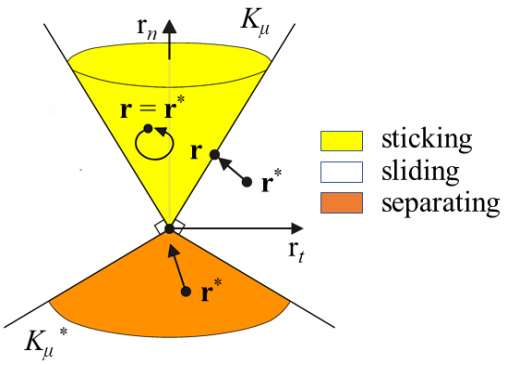

Figure 4. Coulomb cone and contact projection operators

Consequently, we can define the projection operation by:

$$\begin{aligned} &\textit{Separating}: \mathrm{Proj}_{K_\mu}(\mathbf{r}^{\alpha*}) = 0 \quad \text{if} \ \ \mu\left\|\mathbf{r}_t^{\alpha*}\right\| < -r_n^{\alpha*} \\ &\textit{Sticking}: \mathrm{Proj}_{K_\mu}(\mathbf{r}^{\alpha*}) = \mathbf{r}^{\alpha*} \ \ \text{if} \ \ \left\|\mathbf{r}_t^{\alpha*}\right\| < \mu r_n^{\alpha*} \\ &\textit{Sliding}: \mathrm{Proj}_{K_\mu}(\mathbf{r}^{\alpha*}) = \mathbf{r}^{\alpha*} - \left(\frac{\left\|\mathbf{r}_t^{\alpha*}\right\| - \mu r_n^{\alpha*}}{1+\mu^2}\right)\left(\frac{\mathbf{r}_t^{\alpha*}}{\left\|\mathbf{r}_t^{\alpha*}\right\|} - \mu\mathbf{n}^{\alpha}\right) \ \ \text{else} \end{aligned} \tag{42}$$

4.3 *Equilibrium equations of contact points*

The system of equations related to each contact point is:

$$\begin{cases} \bar{\mathbf{K}}\mathbf{d} = \mathbf{F}_{ext} + \mathbf{T}^{\mathrm{T}}\mathbf{r} \\ \mathbf{x} = \mathbf{T}\mathbf{d} + \mathbf{g} \\ \mathbf{r}^{\alpha} = \mathrm{Proj}_{K_\mu}(\mathbf{r}^{\alpha*}) \end{cases} \tag{43}$$

eliminating $\mathbf{d}$ leads to the following system of equations:

$$\begin{cases} \mathbf{x} = \mathbf{T}\bar{\mathbf{K}}^{-1}\mathbf{T}^{\mathrm{T}}\mathbf{r} + \mathbf{T}\bar{\mathbf{K}}^{-1}\mathbf{F}_{ext} + \mathbf{g} \\ \mathbf{r}^{\alpha} = \mathrm{Proj}_{K_\mu}(\mathbf{r}^{\alpha*}) \end{cases} \tag{44}$$

Here, we can define some variables to make the equation more intuitive.

$$\begin{cases} \mathbf{D} = \mathbf{T}\bar{\mathbf{K}}^{-1}\mathbf{T}^{\mathrm{T}} \\ \hat{\mathbf{x}} = \mathbf{T}\bar{\mathbf{K}}^{-1}\mathbf{F}_{ext} + \mathbf{g} \end{cases} \tag{45}$$

where $\mathbf{D}$ is named as the global Delassus operator [42].

For a contact system containing N_c contact points, the contact points are coupled with each other. So, Eq. (44) can be transformed into an implicit system of equations.

$$\boldsymbol{\Psi}^{\alpha}(\mathbf{r},\mathbf{x}) = \begin{Bmatrix} \mathbf{x}^{\alpha} - \mathbf{D}^{\alpha\alpha}\mathbf{r}^{\alpha} - \sum_{\beta=1,\beta\neq\alpha}^{N_c} \mathbf{D}^{\alpha\beta}\mathbf{r}^{\beta} - \hat{\mathbf{x}}^{\alpha} \\ \mathbf{r}^{\alpha} - \mathrm{Proj}_{K_\mu}(\mathbf{r}^{\alpha*}) \end{Bmatrix} = 0 \tag{46}$$

Where $\mathbf{D}^{\alpha\beta} = \mathbf{T}^{\alpha}\bar{\mathbf{K}}^{-1}\mathbf{T}^{\mathrm{T}\beta}$, $\boldsymbol{\Psi}(\mathbf{r},\mathbf{x}) = \begin{bmatrix} \boldsymbol{\Psi}^1 & \cdots & \boldsymbol{\Psi}^{N_c} \end{bmatrix}^{\mathrm{T}} = 0$.

4.4 *Uzawa algorithm*

Uzawa algorithm is a local iterative algorithm to solve implicitly Eq. (46). The calculation procedure mainly includes predictor and corrector for contact forces.

$$\begin{aligned} &Predictor: \mathbf{r}^{\alpha*(i+1)} = \mathbf{r}^{\alpha(i)} - \rho^{(i)}(\mathbf{x}^{\alpha(i)} + \mu\left\|\mathbf{x}_t^{\alpha(i)}\right\|\mathbf{n}^{\alpha}) \\ &Corrector: \mathbf{r}^{\alpha(i+1)} = \mathrm{Proj}_{K_\mu}(\mathbf{r}^{\alpha*(i+1)}) \end{aligned} \tag{47}$$

where i and $i+1$ are iteration numbers.

Algorithm Uzawa algorithm to solve contact problem
assume: $\mathbf{r}^{(0)} = 0$, $\mathbf{g}^{(0)} = (0 \ \ g)$, $\mathbf{x}^{\alpha(0)} = \mathbf{T}\bar{\mathbf{K}}^{-1}\mathbf{F}_{ext} + \mathbf{g}^{(0)}$.
for ($i = 1$ to Θ)
  for ($\alpha = 1$ to N_c)
  $\mathbf{r}^{\alpha*(i+1)} = \mathbf{r}^{\alpha(i)} - \rho^{(i)}(\mathbf{x}^{\alpha(i)} + \mu\left\|\mathbf{x}_t^{\alpha(i)}\right\|\mathbf{n}^{\alpha})$;
  $\mathbf{r}^{\alpha(i+1)} = \mathrm{Proj}_{K_\mu}(\mathbf{r}^{\alpha*(i+1)})$;
  $\mathbf{x}^{\alpha(i+1)} = \mathbf{D}^{\alpha\alpha}\mathbf{r}^{\alpha(i+1)} + \sum_{\beta=1,\beta\neq\alpha}^{N_c} \mathbf{D}^{\alpha\beta}\mathbf{r}^{\beta(i)} + \hat{\mathbf{x}}^{\alpha(i)}$;
  end for
  if ($\frac{\left\|\mathbf{r}^{(i+1)} - \mathbf{r}^{(i)}\right\|}{\left\|\mathbf{r}^{(i+1)}\right\|} \le \varepsilon_g$)
  break ;
  end if
end for
where Θ is the total number of contact iteration. ε_g is a user-defined convergence coefficient.

5. Numerical examples

In this section, we will use three numerical examples to examine the efficiency of the contact analysis while combining the CS-FEM and the bi-potential formulation. For Q4 element, the characteristic length can be defined [29]:

$$h = \sqrt{A_\Omega / N_e} \tag{48}$$

where A_Ω is the area of whole body. The strain energy error e_{error} and the convergence ratio k are defined as:

$$e_{error} = \frac{\left|E_n - E_r\right|}{E_r} \tag{49}$$

$$\mathrm{k} = \frac{\sum_{i=1}^{N_m} \log_{10}(e_{error})_i \left[\log_{10}(h)_i - \frac{1}{N_m}\sum_{i=1}^{N_m}\log_{10}(h)_i\right]}{\sum_{i=1}^{N_m}\left[\log_{10}(h)_i - \frac{1}{N_m}\sum_{i=1}^{N_m}\log_{10}(h)_i\right]^2} \tag{50}$$

where E_n and E_r are the numerical solution and reference solution of the strain energy, respectively. N_m is the number of mesh models. In this work $N_m = 6$.

5.1 *Frictionless contact of the flat and cylindrical bodies*

Consider the contact of a crossed cylindrical-flat arrangement as shown in Fig. 5 (a). The diameter of the cylindrical sample is 12 *mm*. The bottom is a block, and its thickness is 10 *mm* [41]. This problem can be simplified to a plane strain model as shown in Fig. 5 (b).

The displacements are uniformly distributed on top of cylindrical body Ω_1 while a full constraint is applied at the bottom of the flat body Ω_2.

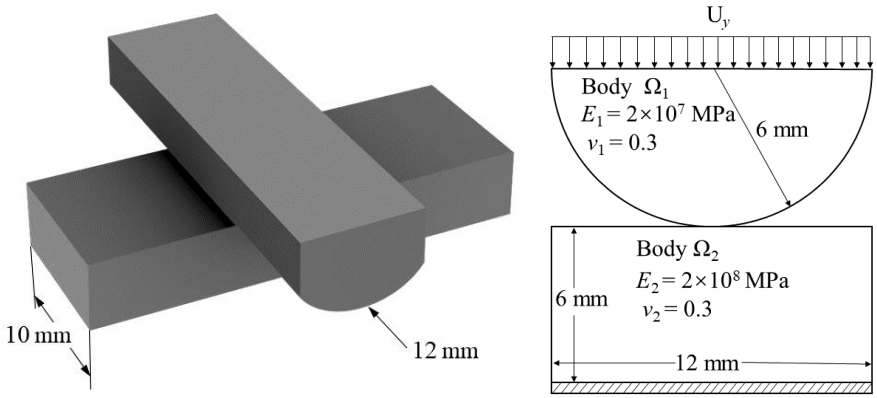

(a) (b)

Figure 5. (a) Model of the crossed cylindrical-flat; (b) Plane strain model

In this example, the Young's modulus and Poisson's ratio of the two bodies are $E_1=2\times10^7$ MPa , $\nu_1=0.3$ and $E_2=2\times10^8$ MPa , $\nu_2=0.3$ respectively. When using different number of nodes and elements are listed in Table 1, the problem domain meshed with quadrangles are given in Fig. 6.

Table 1. The number of nodes and elements of two elastic bodies.

No.	M1	M2	M3	M4	M5	M6	Ref.
Nodes	345	767	1237	1977	3050	4272	36175
Elements	299	699	1151	1871	2920	4118	35755

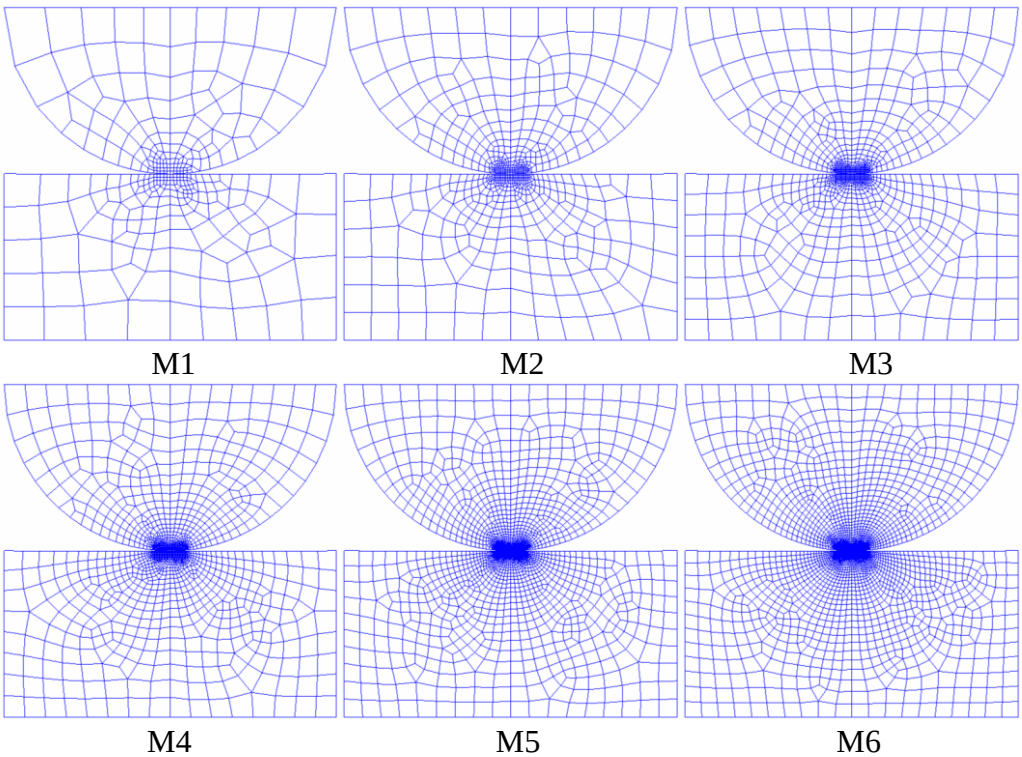

Figure 6. Six different mesh models

5.1.1 *Convergence of strain energy solution*

While choosing $U_y = -0.01\,mm$. Fig. 7 (a) compares the solutions of CS-FEM with different number of smoothing domains. From which we observed that all the solutions converge to the reference solution with the number of degrees of freedom increases. The reference value of the strain energy is obtained by the FEM-Q4 with 35755 quadrilateral elements, as shown in Table 1. And Fig. 7 (b) shows the convergence of the strain energy with respect to the characteristic length. Note that although the accuracy of CS-FEM-1SD is higher, it is unstable when the constraint is insufficient.

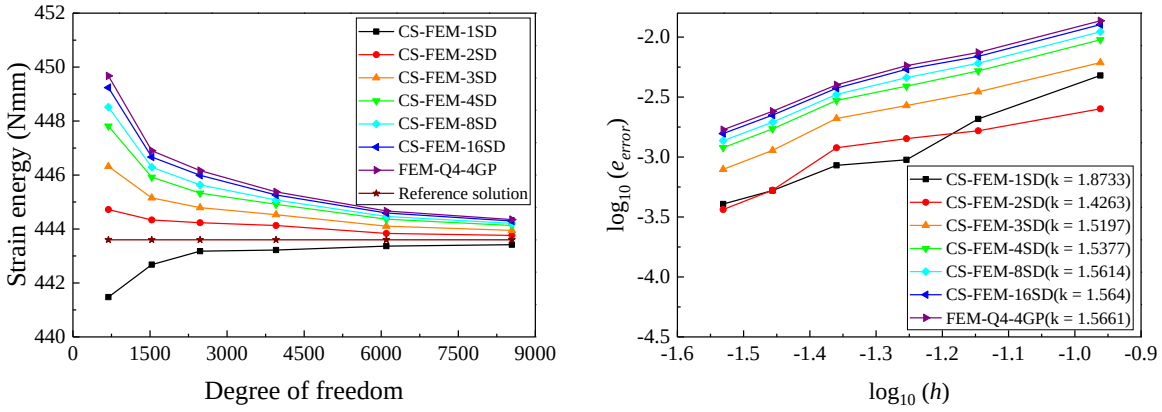

(a) (b)

Figure 7. Numerical solutions (a) and the convergence of strain energy (b)

According to the above figures, several phenomena can be drawn: 1) As the number of degrees of freedom increases, the strain energy solution of CS-FEM-1SD converges from the lower bound and CS-FEM-2SD to 16SD converges from the upper bound. 2) When using the displacement boundary condition, the CS-FEM-1SD provides a lower bound solution while the other models provide upper bound solutions. All the results produced by CS-FEM are more accurate than those of the FEM-Q4. 3) These calculation methods are approximately linear convergent, CS-FEM-1SD has the largest convergence ratio 1.87, the others convergence ratios are from 1.52 to 1.56. 4) The accuracy of CS-FEM-1SD is almost 5 times higher than the FEM-Q4 when using the same quadrilateral elements. CS-FEM-4SD is more stable, and its accuracy is more than 40% higher than the FEM-Q4.

5.1.2 *Hertz contact verification*

In order to investigate the accuracy of the CS-FEM within the bi-potential framework to solve the contact problem, here we adopt the Hertz theoretical solution for comparison [43]. The contact pressure distribution of this model is:

$$p(x) = p_0\left(1-\frac{x^2}{a^2}\right)^{1/2} \tag{51}$$

where x is the distribution of nodes on the contact surface. a and p_0 are the half-width of the contact area and the maximum contact pressure, respectively, which can be expressed as:

$$a = \left(\frac{4Pr}{\pi E^*}\right)^{1/2} \tag{52}$$

$$p_0 = \left(\frac{PE^*}{\pi r}\right)^{1/2} \tag{53}$$

where P is the contact reaction force, E^* is the composite modulus and it can be written as:

$$E^* = (\frac{1-\nu_1^2}{E_1} + \frac{1-\nu_2^2}{E_2})^{-1} \tag{54}$$

r is the relative curvature:

$$r = (\frac{1}{r_1} + \frac{1}{r_2})^{-1} \tag{55}$$

The flat body Ω_2 is an infinite plane and $r_2 \to \infty$. thus, we have $r = r_1$.

For comparison, we use three boundary conditions: $U_{y1} = -0.002\ mm$, $U_{y2} = -0.006\ mm$ and $U_{y3} = -0.01\ mm$. CS-FEM-4SD and the mesh M6 are adopted for discretization. Then, the contact reaction forces corresponding to different boundary conditions are P_1=14983.471 N, P_2=52873.824 N and P_3=96133.574 N respectively. Fig. 8 (a) shows the normal contact stress and the analytical solution of Hertz contact. We can find that the contact reaction force and the normal contact stress will increase when using larger displacements on the boundary. All the solutions agree well with the theoretical solution. Fig. 8 (b) shows the tangential relative slip on the contact surface with respect to the contact length.

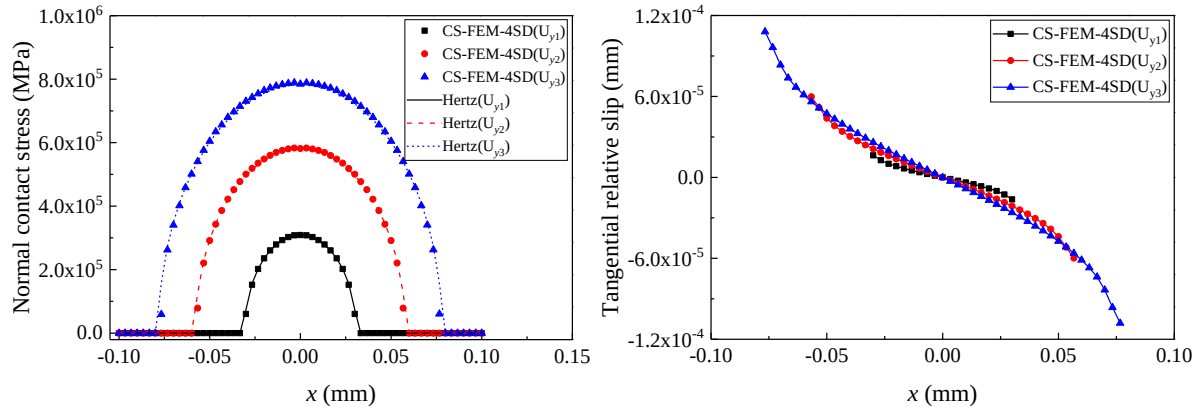

(a) (b)

Figure 8. Normal contact stress (a) and tangential relative slip on the contact surface (b)

5.1.3 *Analysis of penetration*

Fig. 9 shows the penetration of different methods for solving the contact problem within the bi-potential framework. Since the largest penetration produced by CS-FEM-1D is less than $3\times10^{-20}\ mm$, it can be neglected in the calculation.

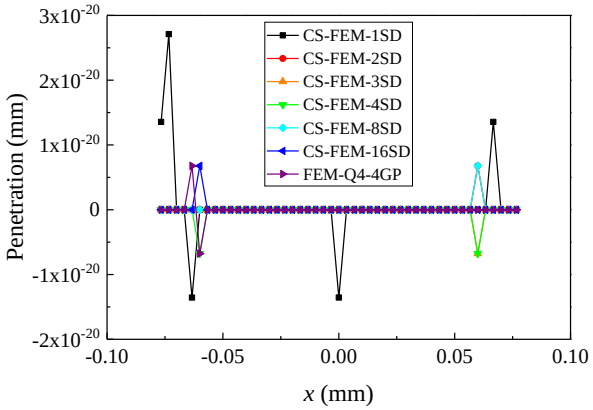

Figure 9. Penetration by using different methods

5.2 *Contact between two elastic bodies*

Considering the two elastic bodies Ω_1 and Ω_2 as shown in Fig. 10. The displacements are uniformly distributed on top of cylindrical body Ω_1 while a full constraint is applied at the bottom of the flat body Ω_2.

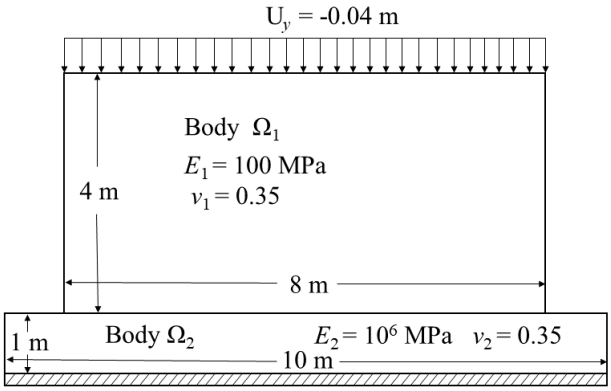

Figure 10. Contact between two elastic bodies

In this example, a plane strain model is used. When using different number of nodes and elements are listed in Table 2, the problem domain meshed with quadrangles are given in Fig. 11.

Table 2. The number of nodes and elements of elastic body Ω_1

No.	M1	M2	M3	M4	M5	M6	Ref.
Nodes	66	231	496	861	1326	1891	51681
Elements	50	200	450	800	1250	1800	51200

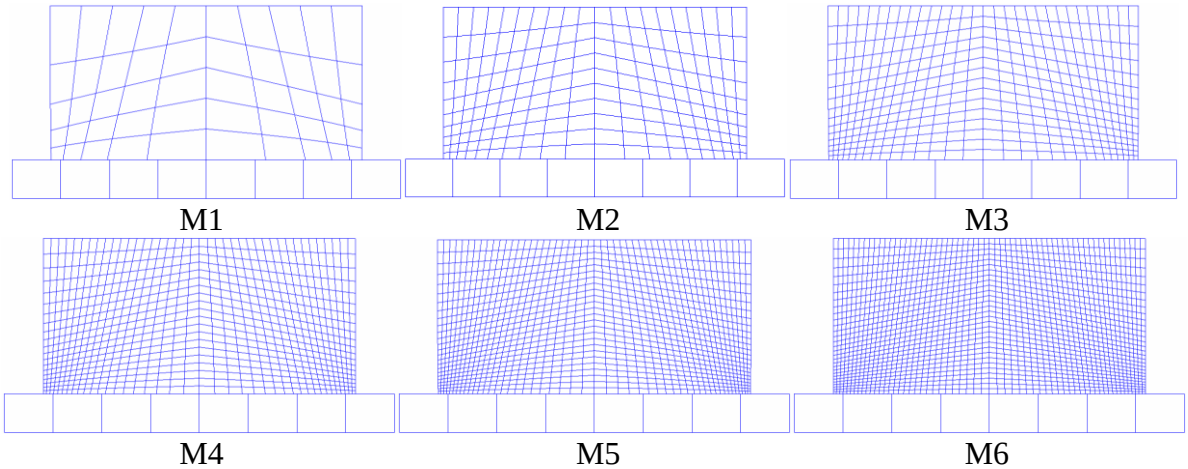

Figure 11. Six different mesh models for two elastic bodies

5.2.1 *Convergence of strain energy solution*

While choosing $U_y = -0.04\,m$ and the friction coefficient μ=0.8. Fig. 7 (a) compares the solutions of CS-FEM with different number of smoothing domains. From which we observed that all the solutions converge to the reference solution with the number of degrees of freedom increases. The reference value of the strain energy is obtained by the FEM-Q4 with 35755 quadrilateral elements, as shown in Table 1. Fig. 7 (b) shows the convergence of the strain

energy with respect to the characteristic length. Note that although the accuracy of CS-FEM-1SD is higher, it is unstable when the constraint is insufficient.

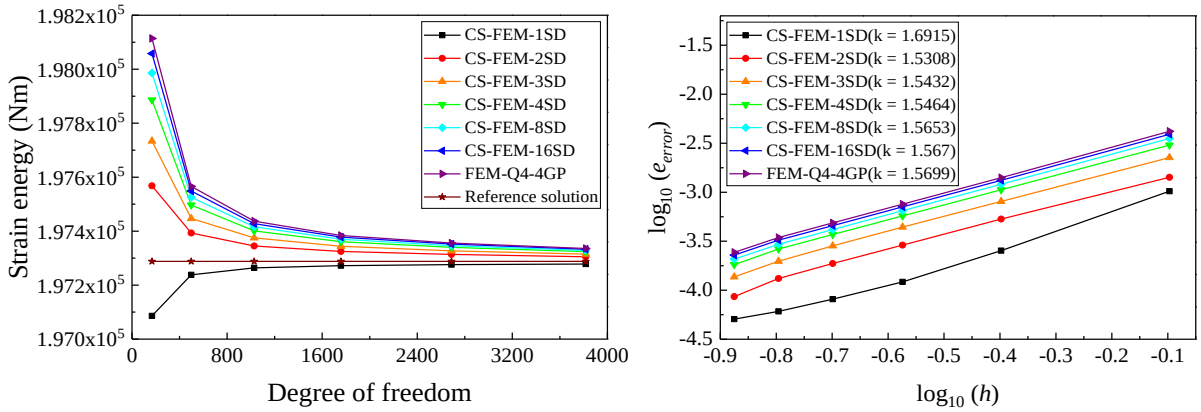

(a) (b)

Figure 12. Numerical solutions (a) and the convergence of strain energy (b)

According to the above description, this example can also get a similar phenomenon to Fig. 7: As the number of degrees of freedom increases, the strain energy solution of CS-FEM converges from the lower bound and the upper bound. When using the displacement boundary condition, the CS-FEM-1SD provides a lower bound solution while the other models provide upper bound solutions. All the results produced by CS-FEM are more accurate than those of the FEM-Q4. The difference is (1) The CS-FEM-1SD has the largest convergence ratio 1.69, the others convergence ratios are from 1.43 to 1.49. (2) When using the same quadrilateral elements, the accuracy of the CS-FEM-1SD is almost 6 times higher than the FEM-Q4. The CS-FEM-4SD is more stable, and its accuracy is more than 30% higher than the FEM-Q4.

5.2.2 *Effect of friction coefficient*

In the following contact analysis, we consider the effect of friction coefficients. The CS-FEM-4SD and M6 model are selected. The friction coefficients are selected as 0.1, 0.15, 0.2, 0.25.

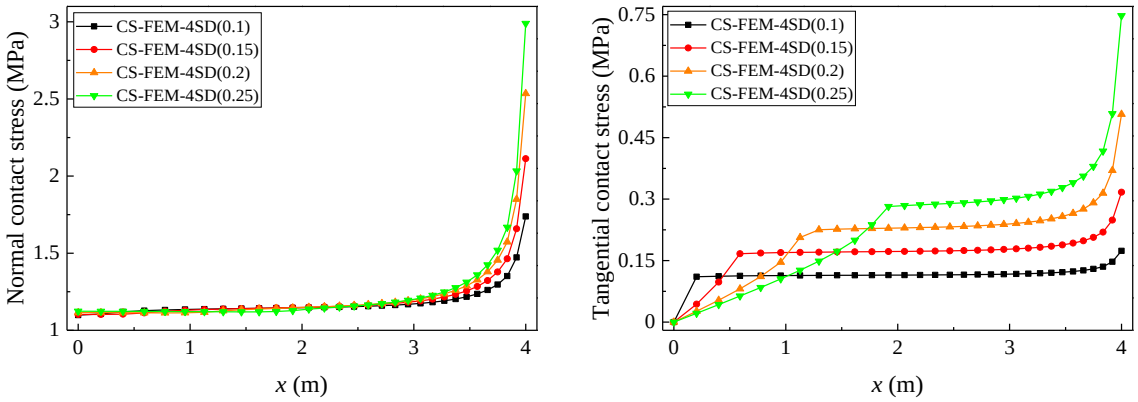

(a) (b)

Figure 13. Normal contact stress (a) and tangential contact stress (b)

Fig. 13 (a) and (b) shows the normal and tangential contact stress of the contact point using different friction coefficients. We can find that the normal contact stress will become higher at the right end, and the tangential contact force will rise first, and then will become higher at the right end when the friction coefficient increases. Fig. 14 (a) and (b) shows the tangential

relative slip and the ratio of contact forces which we can observe the contact states (sticking or sliding) of different contact points.

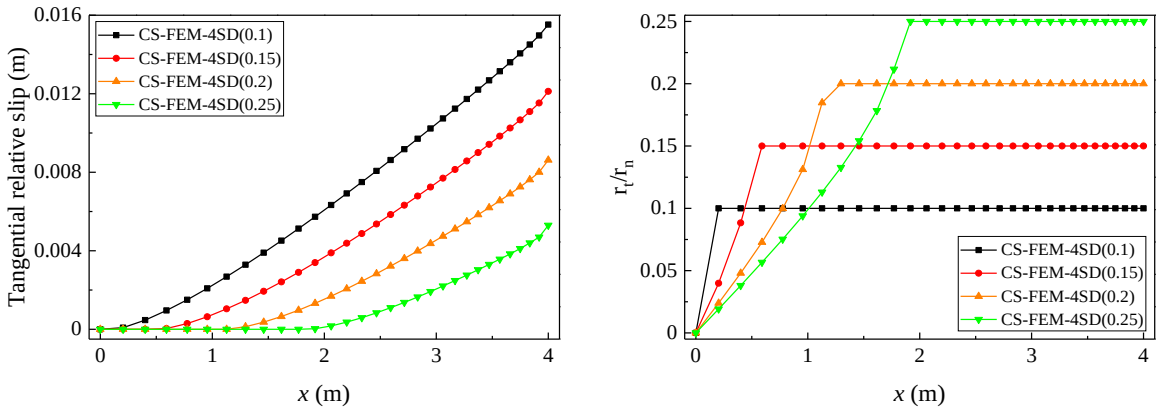

Figure 14. Tangential relative slip (a) and the evolution of contact states (b)

5.2.3 *Analysis of penetration*

Fig. 15 shows the penetration of different cases. Since the largest penetration produced by CS-FEM-1D is less than $8\times10^{-16}m$, it can be neglected in the calculation.

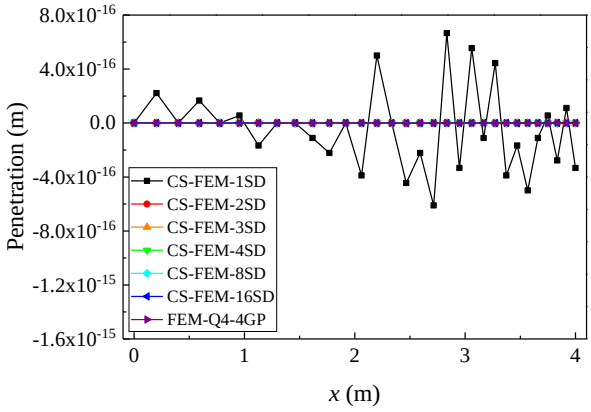

Figure 15. The comparison of penetration when using different methods

5.3 *Contact between two elastic bodies with large slips*

Finally, we consider the two elastic bodies Ω_1 and Ω_2 with large slip as shown in Fig. 16. The displacements are uniformly distributed on top of Ω_1 while a full constraint is applied at the bottom of Ω_2.

In this example, a plane stress model is used. When using different number of nodes and elements as listed in Table 3, the problem domain meshed with quadrangles are given in Fig. 17.

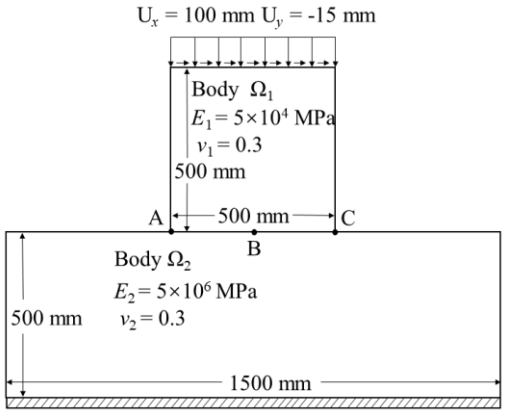

Figure 16. Contact between two elastic bodies with large slip

Table 3. The number of nodes and elements of two elastic bodies Ω1 and Ω2.

No.	M1	M2	M3	M4	M5	M6	Ref.
Nodes	65	214	449	770	1177	1670	27377
Elements	43	172	387	688	1075	1548	26875

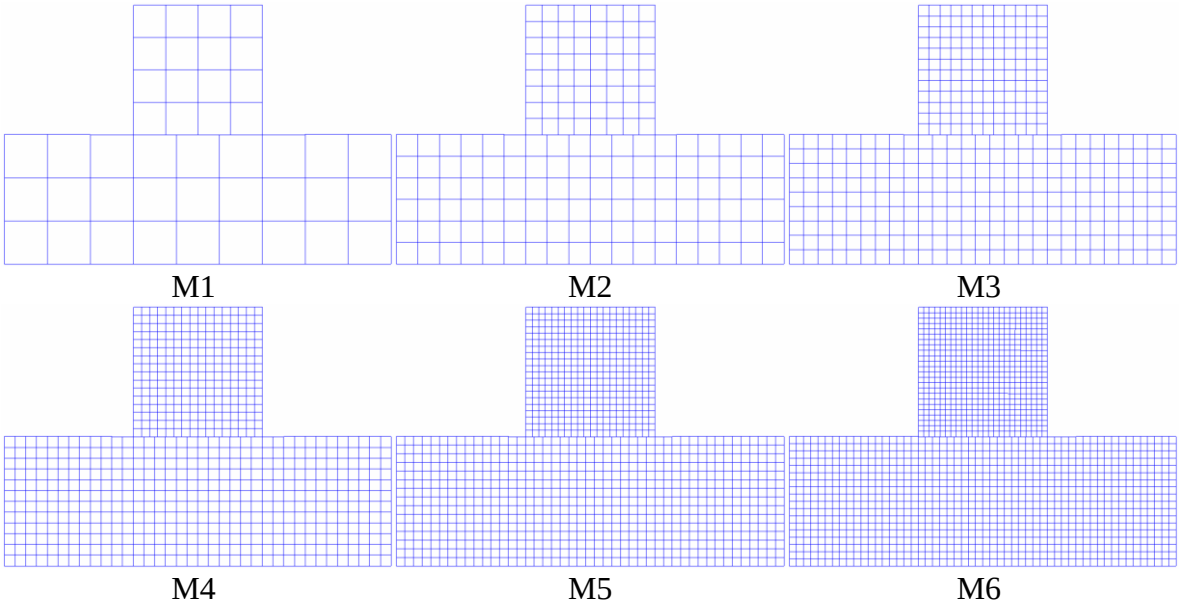

Figure 17. Six different mesh models for two elastic bodies

5.3.1 *Convergence of strain energy solution*

While choosing U_x=100 *mm*, U_y=−15 *mm* and the friction coefficient μ = 0.2. In the following analysis, the multi-step loading is used with 100 load steps. Fig. 18 (a) compares the solutions of CS-FEM with different number of smoothing domains. From which we observed that all the solutions converge to the reference solution with the number of degrees of freedom increases. The reference value of the strain energy is obtained by the FEM-Q4 with 26875 quadrilateral elements, as shown in Table 3. And Fig. 18 (b) shows the convergence of the strain energy with respect to the characteristic length. Note that although the accuracy of CS-FEM-1SD is much higher than the other models, it could be unstable when the constraint is insufficient.

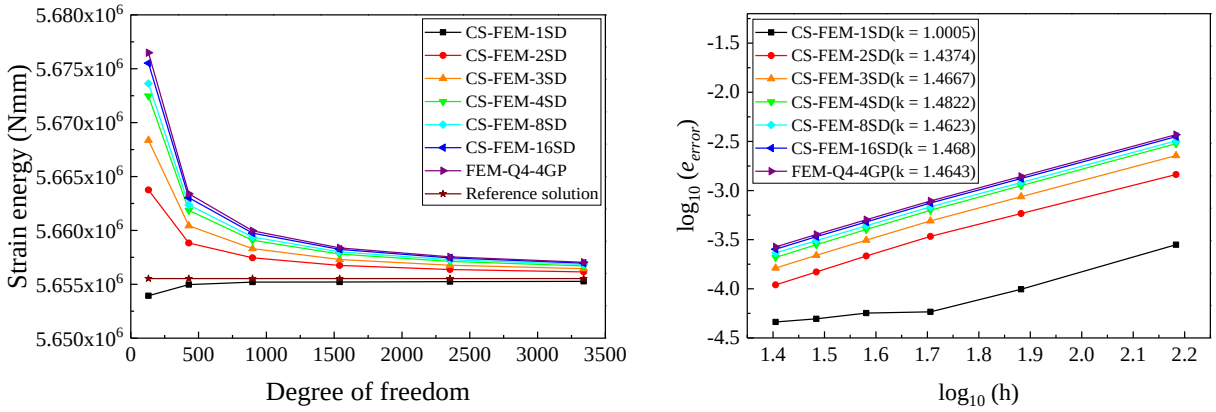

(a) (b)

Figure 18. Numerical solutions (a) and the convergence of the strain energy (b)

According to these figures, we can get the similar phenomenon with the previous two examples: 1) The CS-FEM-1SD has the least convergence ratio 1.0, the others convergence ratios are from 1.43 to 1.48. 2) When using the same quadrilateral elements, the accuracy of the CS-FEM-1SD is almost 5 times higher than the FEM-Q4, and the accuracy of the CS-FEM-4SD is more than 30% higher than the FEM-Q4, Note that the CS-FEM-4SD is more stable.

5.3.2 *Effect of friction coefficient and load step*

In the following contact analysis, the CS-FEM-4SD and M6 model are selected. The friction coefficients are 0.05, 0.1, 0.15, 0.2, respectively. Fig. 19 (a) and (b) shows the normal and tangential contact stress of the contact point using different friction coefficients at load step 100. We can find that as the friction coefficient increases, the upward trend of normal contact stress on the contact surface will be more obvious. The left end of the contact surface decreases while the right end of the contact surface increases. The tangential contact stress will become higher at the right end.

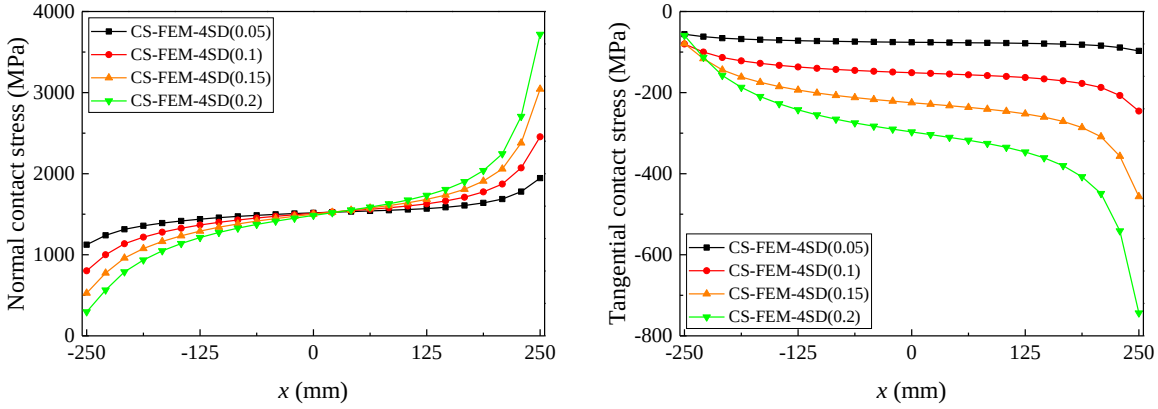

(a) (b)

Figure 19. Normal contact stress (a) and tangential contact stress (b)

We define the friction coefficient is 0.2 to calculate the normal and tangential contact stress of the contact point at different load steps as shown in Fig. 20. We can find that both normal and tangential contact stress increase steadily in the process of loading.

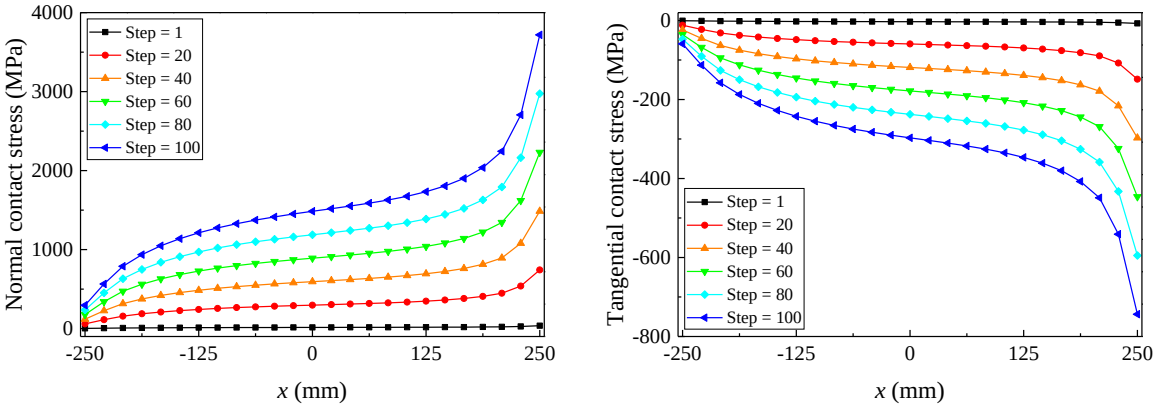

(a) (b)

Figure 20. Normal contact stress (a) and tangential contact stress (b)

Fig. 21 shows the ratio of contact forces which we can observe the contact states (sticking or sliding) of different contact points A, B and C. We can find that during the loading process, they are all in a sliding state, and as the loading progresses, the sliding will be more stable.

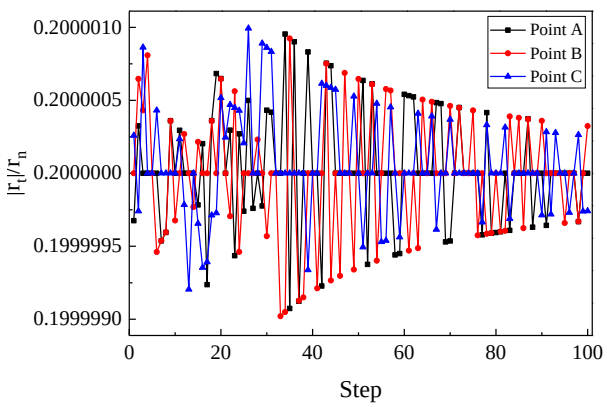

Figure 21. Evolution of contact states

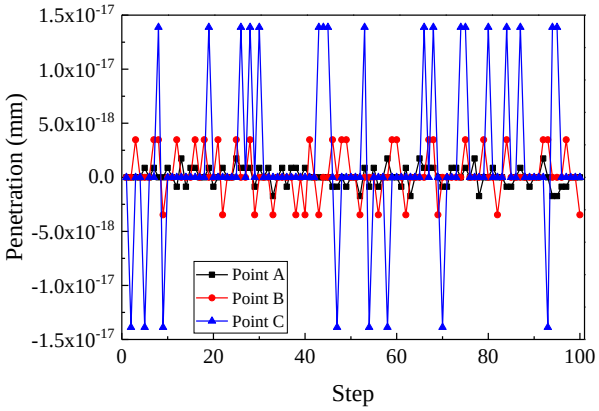

Figure 22. Penetration

5.3.3 *Analysis of penetration*

In the penetration analysis, the CS-FEM-4SD model is selected. The friction coefficient is 0.2. Fig. 22 shows the penetration of the three points A, B and C during the loading process within the bi-potential framework. We can find that the contact force is different, and the corresponding penetration is also different. This is because the accuracy of the contact criterion is controlled by contact forces rather than displacements. We also find that the penetration can reach the order of 1.5×10^{-17} *mm*, which shows a very high precision of our approach.

6. Conclusion

In this work, the CS-FEM is applied with six different smoothing domains based on quadrilateral background elements for solving contact problems. The smoothed Galerkin weak form and the discrete form are derived at first. Then multi-points coupling effect is considered within the bi-potential framework with the exact Signorini-Coulomb condition. The Uzawa algorithm is used to solve the contact force. This method can effectively simulate the three states of separating, sliding and sticking.

Through the study of numerical examples, we can get the following conclusions:

(1) As the number of degrees of freedom increases, the strain energy solution obtained by CS-FEM with different smoothing domains can converge to the reference solution with different smoothing domains. CS-FEM-1SD converges from the lower bound and CS-FEM-2SD to 16SD converges from the upper bound.

(2) When using the displacement boundary condition, the CS-FEM-1SD provides a lower bound solution while the other models provide upper bound solutions. All the results produced by CS-FEM are more accurate than those of the FEM-Q4.

(3) The solution of CS-FEM-1SD is the most accurate. When using the same background elements, its accuracy more than 5 times higher than those of the FEM-Q4. But this model could be unstable when the constraint is insufficient. CS-FEM-4SD has a higher stability in solving contact problems, and its accuracy can be more than 30-40% relative to the FEM-Q4 solution when using the same background elements.

Acknowledgement

We gratefully acknowledge the financial support of the National Natural Science Foundation of China (Grant No. 1177020241), the National Key Research and Development Project of China (Grant No. 2017YFB0703202) and the Fundamental Research Funds for the Central Universities (Grant No.2682019CX42).

References

[1] Wriggers, P. (2002) Computational Contact Mechanics, John Wiley & Sons.

[2] Johnson, K. L. (1985) Contact mechanics, *Journal of Tribology* **108**, 464.

[3] Zienkiewicz, O. C. and Taylor, R. L. (2005) *The Finite Element Method*.

[4] Bathe, K. J. and Chaudhary, A. (1985) A solution method for planar and axisymmetric contact problems. *International Journal for Numerical Methods in Engineering* **21**, 65-88.

[5] Weyler, R., Oliver, J., Sain, T., and Cante, J. C. (2012) On the contact domain method: a comparison of penalty and lagrange multiplier implementations, *Computer Methods in Applied Mechanics & Engineering* **205**, 68-82.

[6] Biotteau, E. and Ponthot, J. P. (2012) Modeling frictional contact conditions with the penalty method in the extended finite element framework, *Journal of Business Ethics*.

[7] Okabe, M. and Kikuchi, N. (2010) Penalty method to a two-body contact problem, *Engineering Mechanics*, 700-703.

[8] Belytschko, T. and Neal, M. O. (1991) Contact-impact by the pinball algorithm with penalty and lagrangian methods, *International Journal for Numerical Methods in Engineering* **31**, 547-572.

[9] Carpenter, N. J., Taylor, R. L., and Katona, M. G. (1991) Lagrange constraints for transient finite element surface contact, *International Journal for Numerical Methods in Engineering* **32**, 103-128.

[10] Pitkaranta, J. (1980) The finite element method with lagrange multipliers, *Mathematics of Computation* **37**, 13-30.

[11] Baillet, L., and Sassi, T. (2002) Finite element method with lagrange multipliers for contact problems with friction, *Comptes Rendus Mathematique* **334**, 917-922.

[12] H. Barbosa. (1991) The finite element method with lagrange multipliers on the boundary: circumventing the Babuka-Brezzi condition, *Computer Methods in Applied Mechanics & Engineering* **85**, 109-128.

[13] Farnood Gholami, Mostafa Nasri, József Kövecses, and Marek Teichmann. (2016) A linear complementarity formulation for contact problems with regularized friction. *Mechanism & Machine Theory* **105**, 568-582.

[14] Li, J., Zhang, H., and Pan, S. (2010) A second-order cone linear complementarity approach for contact problems with orthotropic friction law, *Chinese Journal of Solid Mechanics* **31**, 109-118.

[15] Li, J., Pan, S., and Zhang, H. (2009) A second-order cone linear complementarity approach for three-dimensional frictional contact problems, *Lixue Xuebao/Chinese Journal of Theoretical and Applied Mechanics* **41**, 869-877.

[16] Yue, J. H., Liu, G. R., Li, M., and Niu, R. P. (2018) A cell-based smoothed finite element method for multi-body contact analysis using linear complementarity formulation, *International Journal of Solids and Structures*, 110-126.

[17] De Saxcé, G. and Feng, Z. Q. (1991) New inequality and functional for contact with friction: the implicit standard material approach, *Mechanics of Structures and Machines* **19**, 301-325.

[18] De Saxcé, G. and Feng, Z. Q. (1998) The bipotential method: A constructive approach to design the complete contact law with friction and improved numerical algorithms, *Mathematical and Computer Modelling* **28**, 225-245.

[19] Joli, P., and Feng, Z. Q. (2008) Uzawa and Newton algorithms to solve frictional contact problems within the bi-potential framework, *International Journal for Numerical Methods in Engineering* **73**, 317-330.

[20] Feng, Z. Q., Magnain, B., and Cros, J. M. (2006) Solution of large deformation impact problems with friction between Blatz-Ko hyperelastic bodies, *International Journal of Engineering Science* **44**, 113-126.
[21] Feng, Z. Q., Peyraut, F., and Labed, N. (2003) Solution of large deformation contact problems with friction between Blatz-Ko hyperelastic bodies, *International Journal of Engineering Science* **41**, 2213-2225.
[22] Ning, P., Feng, Z. Q., Quintero, J. A., Zhou, Y.J,, and Peng, L. (2018) Uzawa algorithm to solve elastic and elastic–plastic fretting wear problems within the bipotential framework, *Computational Mechanics* **62**, 1327-1341.
[23] Peng, L., Feng, Z. Q., Joli, P., Renaud, C., and Xu, W. Y. (2019) Bi-potential and co-rotational formulations applied for real time simulation involving friction and large deformation. *Computational Mechanics* **64**, 611-623.
[24] Eck, C., Steinbach, O., and Wendland, W. L. (1999) A symmetric boundary element method for contact problems with friction, *Mathematics and Computers in Simulation* **50**, 43-61.
[25] Zhu, C. (1995) A new boundary element/mathematical programming method for contact problems with friction, *Communications in Numerical Methods in Engineering* **11**, 683-690.
[26] Li, Y., Liu, G. R., Dai, K. Y., Luan, M., Zhong, Z. H., Li, G. Y., and Han, X. (2007) Contact analysis for solids based on linearly conforming radial point interpolation method, *Computational Mechanics* **39**, 537-554.
[27] Rabczuk, T., and Belytschko, T. (2007) A three-dimensional large deformation meshfree method for arbitrary evolving cracks, *Computer Methods in Applied Mechanics and Engineering* **196**, 2777-2799.
[28] Rabczuk, T., and Ren, H. (2017) A peridynamics formulation for quasi-static fracture and contact in rock, *Engineering Geology*, 42-48.
[29] Liu, G. R., and Trung, N. T. (2010) *Smoothed Finite Element Methods*.
[30] Liu, G. R., Dai, K. Y., and Nguyen, T. T. (2007) A smoothed finite element method for mechanics problems, *Computational Mechanics* **39**, 859-877.
[31] Liu, G. R., Nguyen, T. T., Dai, K. Y., and Lam, K. Y. (2007) Theoretical aspects of the smoothed finite element method (SFEM), *International Journal for Numerical Methods in Engineering* **71**, 902-930.
[32] Thaihoang, C., Nguyenthanh, N., Nguyenxuan, H., Rabczuk, T., and Bordas, S. (2011) A cell — based smoothed finite element method for free vibration and buckling analysis of shells, *Ksce Journal of Civil Engineering* **15**, 347-361.
[33] Nguyenthoi, T., Rabczuk, T., Lamphat, T., Hohuu, V., and Phungvan, P. (2014) Free vibration analysis of cracked Mindlin plate using an extended cell-based smoothed discrete shear gap method (XCS-DSG3), *Theoretical and Applied Fracture Mechanics*, 150-163
[34] Li, E., He, Z. C., Xu, X., and Liu, G. R. (2015) Hybrid smoothed finite element method for acoustic problems, *Computer Methods in Applied Mechanics and Engineering*, 664-688.
[35] Nguyenxuan, H., Tran, L. V., Nguyenthoi, T., and Vudo, H. C. (2011) Analysis of functionally graded plates using an edge-based smoothed finite element method, *Composite Structures* **93**, 3019-3039.
[36] Dai, K. Y., and Liu, G. R. (2007) Free and forced vibration analysis using the smoothed finite element method (SFEM), *Journal of Sound and Vibration* **301**, 803-820.
[37] He, T. (2018) Towards straightforward use of cell-based smoothed finite element method in fluid–structure interaction, *Ocean Engineering*, 350-363.
[38] Li, S., Cui, X., and Li, G. (2017) Multi-physics analysis of electromagnetic forming process using an edge-based smoothed finite element method, *International Journal of Mechanical Sciences*, 244-252.
[39] Li, Y., Zhang, G., Liu, G. R., Huang, Y. N., and Zong, Z. (2013) A contact analysis approach based on linear complementarity formulation using smoothed finite element methods, *Engineering Analysis with Boundary Elements* **37**, 1244-1258.
[40] Li, Y., Liu, G. R., and Zhang, G. (2011) An adaptive NS/ES-FEM approach for 2D contact problems using triangular elements, *Finite Elements in Analysis and Design* **47**, 256-275.
[41] Klarbring, A. (1992) Mathematical programming and augmented Lagrangian methods for frictional contact problems, *Proceedings Contact Mechanics International Symposium*, 409-422.
[42] Francavilla, A. and Zienkiewicz, O. C. (1975) A note on numerical computation of elastic contact problems, *International Journal for Numerical Methods in Engineering* **9**, 913-924.
[43] Mccoll, I. R., Ding, J., and Leen, S. B. (2004) Finite element simulation and experimental validation of fretting wear, *Wear* **256**, 1114-1127.